

Marquette University

e-Publications@Marquette

Mechanical Engineering Faculty Research and
Publications

Mechanical Engineering, Department of

1-2019

Investigation of Void Formation in Friction Stir Welding Of 7N01 Aluminum Alloy

Xingxin Zhao

Beijing Jiaotong University

Jianmin Han

Beijing Jiaotong University

Joseph P. Domblesky

Marquette University, joseph.domblesky@marquette.edu

Zhiyong Yang

Beijing Jiaotong University

Zhiqiang Li

Beijing Jiaotong University

See next page for additional authors

Follow this and additional works at: https://epublications.marquette.edu/mechengin_fac



Part of the [Mechanical Engineering Commons](#)

Recommended Citation

Zhao, Xingxin; Han, Jianmin; Domblesky, Joseph P.; Yang, Zhiyong; Li, Zhiqiang; and Liu, Xiaolong, "Investigation of Void Formation in Friction Stir Welding Of 7N01 Aluminum Alloy" (2019). *Mechanical Engineering Faculty Research and Publications*. 243.

https://epublications.marquette.edu/mechengin_fac/243

Authors

Xingxin Zhao, Jianmin Han, Joseph P. Domblesky, Zhiyong Yang, Zhiqiang Li, and Xiaolong Liu

Marquette University

e-Publications@Marquette

Mechanical Engineering Faculty Research and Publications/College of Engineering

This paper is NOT THE PUBLISHED VERSION; but the author's final, peer-reviewed manuscript. The published version may be accessed by following the link in the citation below.

Journal of Manufacturing Processes, Vol. 37 (January 2019): 139-149. [DOI](#). This article is © Elsevier and permission has been granted for this version to appear in [e-Publications@Marquette](#). Elsevier does not grant permission for this article to be further copied/distributed or hosted elsewhere without the express permission from Elsevier.

Investigation of Void Formation in Friction Stir Welding Of 7N01 Aluminum Alloy

Yingxin Zhao

School of Mechanical Electronic & Control Engineering, Beijing Jiaotong University, Beijing, China

Jianmin Han

School of Mechanical Electronic & Control Engineering, Beijing Jiaotong University, Beijing, China

Joseph P. Domblesky

Department of Mechanical Engineering Marquette University, Milwaukee, WI

Zhiyong Yang

School of Mechanical Electronic & Control Engineering, Beijing Jiaotong University, Beijing, China

Zhiqiang Li

School of Mechanical Electronic & Control Engineering, Beijing Jiaotong University, Beijing, China

Xiaolong Liu

School of Mechanical Electronic & Control Engineering, Beijing Jiaotong University, Beijing, China

Abstract

Friction Stir Welding (FSW) is a solid state joining process that is widely used to produce high integrity aluminum weldments for a variety of industries. While extensive work has been conducted to understand flow behavior, much less research has been performed to identify how void defects form and how to predict them. In the present study, the relationship between rotation speed, plasticized region, and defect formation was investigated. To analyze how tunneling and cavity type void defects form during FSW, a 3-D Computational fluid dynamics(CFD) model based on the Fluent software code was used to simulate butt welding. The CFD model was validated using temperature measurements and marker materials from FSW welds made on 12 mm thick 7N01 aluminum alloy plate. Analysis of the simulation results showed that the formation of tunneling defects at lower rotation speeds correlated to a large variation in the size of the plasticized region over the plate thickness. At higher rotation speeds, analysis of material flowlines indicated an imbalance in rotational and longitudinal flow around the pin which resulted in a cavity type defect. It is considered that the results can be used to compare different weld schedules and be used to assess the likelihood of void formation in an actual weld using a CFD model.

Keywords

Friction stir welding, Void defect, Material flow, Butt weld, Rotation speed, Marker Insert Technique

1. Introduction

Friction stir welding (FSW) is a solid-state joining process that is widely used to fabricate aluminum weldments used in the aerospace, automotive, rail, and maritime sectors. In contrast to other fusion welding processes, heat generation is based on friction and deformation-heating caused by a rotating tool such that the maximum temperature remains below the base metal melting point. Because coalescence occurs while material is in the solid state, most of the defects caused by solidification in the weld zone can be avoided [1]. However, due to the fact that the metal is heated and transformed into a plasticized state, the complex stirring action created by the welding tool can lead to the formation of flow related defects such as cavities [2], tunnels [3,4], and grooves [5]. Such void defects have a deleterious effect on weld integrity and test results have shown that tensile properties can be reduced by as much as 70% in comparison to sound welds [6,7].

Although material flow in FSW continues to be actively studied, a number of researchers have begun to investigate how void defects form. Kim et al. [8] developed processing maps for 4 mm ADC12 butt welds and reported that cavity type defects formed when insufficient or excess heat input was used. Their results also showed that the axial force could reduce the void size at lower heat input but was less effective at higher heat conditions. While cavity formation at high heat input was attributed to “abnormal stirring”, the formation mechanism were not elucidated. In contrast, Dawood et al. [9] studied different pin profiles using 4 mm thick AA6061 plate. They reported defects were somewhat dependent on the pin geometry but did not provide a detailed analysis. While existing research provides some insights regarding the potential causes of cavity and tunnel void type defects, additional work is needed to identify representative process conditions that indicate a strong likelihood of defect generation. Additionally, little work on defect formation appears to have been conducted using plate thicknesses in excess of 4 mm.

While physical experiments are a useful tool for studying defect formation, due to the cost and difficulty of making detailed observations regarding process behavior, it is often preferable to use finite element (FE) simulation based models. The use of FE-based process models not only makes it possible to obtain full-field descriptions of temperature and material flow as a function of time, but also facilitates an analysis of how different process conditions indicate defect formation. While a number of workers have used computational solid mechanics models based on the Lagrangian formulation, such analyses tend to be computationally

expensive because of excessive mesh distortion. An additional difficulty arises from the fact that, lacking suitable constitutive models, the formation of void defects are difficult to model. As a result, computational fluid dynamics (CFD) models based on the Eulerian formulation are increasingly employed where the base metal is considered to be an incompressible non-Newtonian fluid rather than a deformable solid. Colegrove et al. [[10], [11], [12]] developed a series of 2D and 3D process models using the Fluent software code in an effort to analyze the material flow field in the vicinity of the tool. They reported that the model over-predicted deformation zone size, weld temperature, and power but noted that this could be corrected by using a slip flow model or a temperature dependent material viscosity.

While CFD based simulation has proven to be a useful tool for analyzing the temperature distribution and material flow fields that develop in FSW, to date relatively few models have been used to investigate the formation of void type defects. Several researchers have shown that the generation of void defects had a strong correlation with the occurrence of a region of diminishing flow-stress [13], velocity [14], pressure [15], and friction force [16] behind the tool pin. When the material in front of the tool pin moved to this region from the retreating side, the material speed significantly decreased due to the insufficient driving/friction force, and it became difficult for the material to move to the advancing side along the circular path.

In the present study, the relationship between tool rotation speed and the formation of flow related void defects was investigated. It is generally accepted that the primary cause of void type defects is heat input, consequently rotation speed was selected due to the fact that it is considered to be responsible for most of the heat input that is generated during FSW [17]. Experimental FSW welds were made using 12 mm thick 7N01 aluminum plates to establish a range of rotation speeds which produced tunneling and cavity void type defects as well as sound welds. A 3D finite element model based on the Fluent CFD software was also validated and used to analyze the steady-state temperature field and material flow behavior for each of the rotation speeds considered. The formation of both void defects is discussed based on variations observed in the temperature and flow fields on the basis of results obtained from the FE simulation model.

2. Experimental procedure

2.1. Work-piece and FSW tool material

The base metal used in the investigation consisted of 7N01 aluminum alloy hot rolled plate in the as-received condition. The nominal chemical composition of the 7N01 plate is shown in Table 1. This alloy is based on the Al-Mg-Zn system and was selected because it is widely used in high speed rail systems. The base metal pieces were prepared by cutting 300 mm × 100 mm sections from 12 mm thick plate using a wire electrical discharge machine.

Table 1. Chemical composition (expressed in wt %) of the 7N01 aluminum alloy used in the study.

Al	Mg	Zn	Si	Fe	Mn	Cr	Ti
Bal	1.11	4.04	0.1	0.17	0.36	0.17	0.04

To characterize the mechanical properties of the base metal, a series of tensile tests were conducted at different temperatures using a constant strain rate of $2 \times 10^{-3} \text{ s}^{-1}$ according GB/T 228.1-2010 and GB/T 4338-2006. Fig. 1 (a) shows the yield stress of the 7N01 plate material as a function of test temperature and the curve can be seen to follow a sigmoidal shape. Thermal properties were also measured and are shown in Fig. 1(b) as a function of temperature. Specific heat was measured by differential scanning calorimetry using an Al_2O_3 reference specimen while thermal conductivity was obtained using the flash method. The melting

temperature of 7N01 alloy is 899 K and the specific heat and thermal conductivity both demonstrated a sharp peak at 580 K which is indicative of a phase transformation.

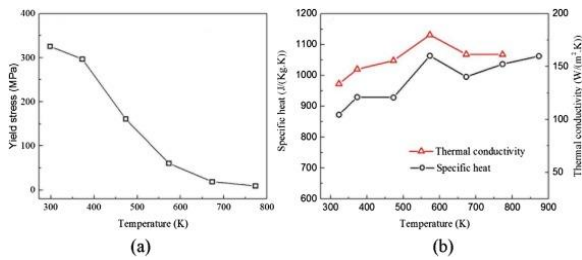


Fig. 1. Experimentally measured (a) yield stress and (b) thermal properties of 7N01 aluminum-alloy shown as a function of temperature.

2.2. Experimental welding procedure

As part of the study, a series of butt welds were made using a China Center 3LM gantry type FSW machine equipped with a work-holding fixture and steel backing plate. Each weld was made along the entire length of the base metal plates so that no entrance or exit holes were generated Fig. 2 shows the geometry of the welding tool which was machined from hardened H13 tool steel and included a right hand threaded pin. The tool shoulder was 37 mm in diameter and had a concave profile machined on the contact surface. The pin consisted of an 11.5 mm long cone having a 14.8 mm diameter near the shoulder and 10° taper. Trapezoidal threads having a 2 mm width screw groove and 30° thread angle were also machined on the surface of tool pin. All welds were made using a constant travel speed of 300 mm/min. A plunge depth of 0.2 mm was employed and a tilt angle of 2.5° was applied to the tool during each welding pass. The rotation speed was varied from 200 rpm to 500 rpm in 150 rpm increments. A complete summary of the welding parameters used is given in Table 2.

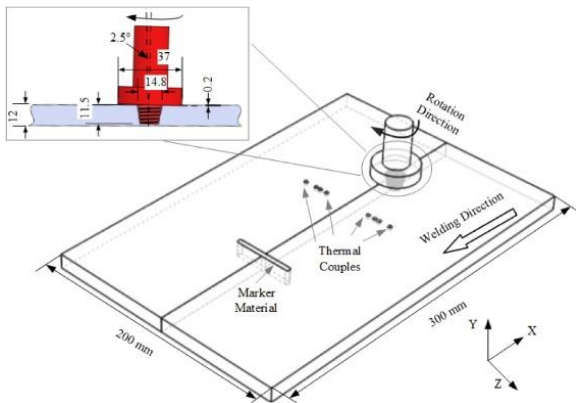


Fig. 2. Schematic diagram of the friction stir welding setup with marker material and thermocouple locations indicated. All dimensions are given in mm.

Table 2. Summary of weld schedules parameters used to make the experimental FSW welds.

Experiment	Rotation Speed (rpm)	Welding Speed (mm/min)	Plunge Depth (mm)	Tool Tilt (°)	Designation
1	200	300	0.2	2.5	Cold welding (CW)
2	350	300	0.2	2.5	Medium welding (MW)
3	500	300	0.2	2.5	Hot welding (HW)

Temperature was recorded during each welding pass using eight K-type thermocouples. Each thermocouple was embedded in a 10.0 mm deep hole that had been drilled from the bottom surface of the plate. The thermocouples were symmetrically mounted along a perpendicular line at distances of 20.0, 24.0, 28.0 and

35.0 mm away from the joint as depicted in Fig. 2. Material flow for the medium welding condition was observed using the Marker Insert Technique (MIT). In order to match the base metal properties, two 4 mm wide \times 20 mm long pieces were cut from a 5 mm thick 7N01 aluminum plate. Micro Arc Oxidation (MAO) was then used to deposit a dark aluminum oxide layer on the top surface of one of the pieces. A 10 mm deep \times 20 mm long transverse slot, centered at the weld joint, was then cut in the two base metal pieces using an end milling machine. The two 20 mm long inserts were then placed in the slot such that the surface with the oxide layer was positioned at a depth of 5 mm from the top surface of the base metal.

At the completion of welding, a computer tomography (CT) machine set in transmission mode was used to scan the weldment containing the inserts and make an image of the resulting marker distribution on the X-Z plane. Transverse cuts were then made at mid-length and at 120 mm from the leading edge of each weldment to expose the nugget cross-sections. The cross-sections were polished using increasing grades of emery paper and a diamond compound after which they were etched using Keller's reagent (100 ml of aqueous solution: 0.5 ml of hydrofluoric acid, 1.5 ml of hydrochloric acid, and 2.5 ml of nitric acid). Macrographs of the polished cross-sections were then made using a CCD camera.

3. Experimental results

Fig. 3 shows the resulting cross-sectional macrostructures taken at 120 mm from the leading edge of the weldment for the three welding conditions that were used. While full penetration was achieved in all three cases, void defects are clearly evident for the CW and HW conditions. Some differences in the nugget geometry can also be seen. For the cold and medium conditions, the nugget outline is symmetric about the centerline and closely follows the tapered pin geometry.

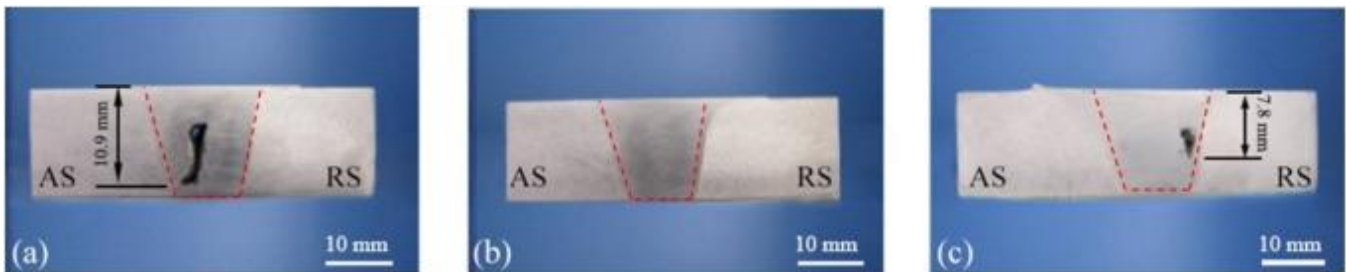


Fig. 3. Cross-sectional macrostructures of the joint for (a) cold welding, (b) medium welding, and (c) hot welding conditions.

Examining Fig. 3a it can be seen that a 6.7 mm high and 1.9 mm in wide tunnel defect formed along the centerline in the bottom half of the nugget for the cold welding condition. This type of defect is usually attributed to insufficient heating and plasticized zone development. The resulting lack of flowability indicates that the material in the bottom half of the weld line was not stirred but was merely extruded as the tool passed.

As the rotation speed of the tool increased, the defect disappeared under the medium welding condition and a sound weld resulted as can be seen in Fig. 3b. It has been shown that about 80% of heat is generated at the tool shoulder while the remaining amount is distributed along the length of the pin [18]. Considering the pin taper, and the fact that the relative surface speed between the tool and the material will be proportional to the pin diameter d , it can be considered that heat generation will decrease with diameter and be a minimum at the tip of the pin.

However, at the 500 rpm rotational speed, it can be seen that a 3.2 mm high by 1.3 mm wide cavity defect developed adjacent to the nugget boundary of mid-thickness of the plate (Fig. 3c). An unbalanced nugget can be seen to have developed under the hot welding condition and is skewed towards the AS. The reason for this asymmetry is that the higher rotation speed results in more material passing around the advancing side than the

retreating side [19]. While the presence of a cavity suggests the possibility of local turbulent flow conditions, this is unlikely as the viscosity of the plasticized material is still relatively high. This is supported by noting that Reynolds numbers in the vicinity of the pin and nugget are low [20] and on the order of 10^{-4} to 10^{-3} which is consistent with laminar flow. This defect likely formed on the RS due to excessive material softening near the periphery of the weld nugget and a large thermal gradient caused by the higher rotation speed [21]. However, this does not take into account the material flow field.

4. Numerical modeling

To study the differences in temperature and material flow that existed between each welding condition and analyze subsequent defect formation, a 3D thermo-fluid model of the FSW set-up was developed using the commercially available Fluent CFD code. Because void formation primarily occurs during steady-state welding conditions, and all experimental welds were made full-length, the entry and exit stages were not considered. Consequently, the simulation effort focused on analyzing the temperature distribution and material flow after welding conditions had reached a quasi-steady state. As details regarding Fluent are well known and available elsewhere in the literature [[22], [23], [24]], only an overview of the model is provided here.

4.1. FSW model description and mesh scheme

A schematic representation of the FSW simulation model is shown in Fig. 4. In the Fluent simulation model, the tool is assumed to rotate about a stationary position at a fixed rotation speed and the aluminum base metal flows through the fluid domain at a constant volumetric rate. The top, side and bottom surfaces of the base metal pieces were specified as the boundaries of the fluid domain. Flow direction was defined by the surfaces marked inlet and outlet in Fig. 4 and was specified to be equal to 300 mm/min such that the relative velocities were identical to the travel speed used to make the experimental welds. The origin point was defined to be coincident with the intersection of the tool rotational axis and the top surface of the work-piece. The fluid domain was discretized using 280,537 tetrahedron elements having 1 mm edge lengths and 71,851 nodes. A finer mesh with 0.6 mm edge lengths was applied in the vicinity of the tool/work-piece (T/W) boundary. A 0.5 mm thick boundary mesh layer consisting of 5 cells was also defined at the T/W boundary to reduce mesh distortion.

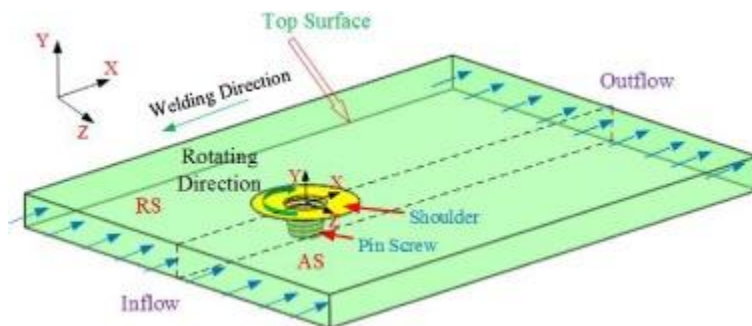


Fig. 4. Schematic illustration of the FSW simulation model used in the study.

4.2. Governing equations

The continuity conservation of momentum and energy equation-governing incompressible single-phase flow can be expressed as:

$$(1) \nabla \cdot (\rho \vec{v}) = 0$$

$$(2) \rho \left(\frac{\partial \vec{v}}{\partial t} + \vec{v} \cdot \nabla \vec{v} \right) = -\nabla p + \nabla \cdot (\mu (\nabla \vec{v} + \nabla \vec{v}^T))$$

$$(3) \rho \left(\frac{\partial(c_p T)}{\partial t} + \nabla \cdot (\vec{v} C_p T) \right) = \nabla \cdot (k \nabla T)$$

Where ρ is the density, μ is the non-Newtonian viscosity, p is the pressure, \vec{v} is the material flow velocity, C_p is the specific heat, k is the thermal conductivity, and T is the temperature.

4.3. Material constitutive model

As the aluminum base metal is considered to be a non-Newtonian fluid in the Fluent simulation model, elastic behavior and strain hardening were neglected. This assumption is reasonable for aluminum alloys based on the fluid analogy and the relatively large strain values that result during FSW [20]. Viscosity was specified to be temperature and strain rate dependent and was calculated using the following formulation [25],

$$(4) \mu = \frac{\sigma(T, \dot{\epsilon})}{3\dot{\epsilon}}$$

Where σ is the material flow stress proposed by Sheppard and Jackson [26] and can be stated as:

$$(5) \sigma(T, \dot{\epsilon}) = \frac{1}{\eta} \ln \left\{ \left(\frac{Z(T, \dot{\epsilon})}{A} \right)^{1/n} + \left[1 + \left(\frac{Z(T, \dot{\epsilon})}{A} \right)^{2/n} \right]^{1/2} \right\}$$

Where A , η and n are material constants and Z is the Zener-Hollomon parameter, which is given by:

$$(6) Z(T, \dot{\epsilon}) = \dot{\epsilon} \exp \left(\frac{Q}{RT} \right)$$

Where R is the universal gas constant, Q is the deformation activation energy, and $\dot{\epsilon}$ is the effective strain rate defined as:

$$(7) \dot{\epsilon} = \left(\frac{2}{3} e_{ij} e_{ij} \right)^{\frac{1}{2}}$$

Where e_{ij} is the strain rate tensor and is given as

$$(8) e_{ij} = \frac{1}{2} \left(\frac{\partial v_i}{\partial x_j} + \frac{\partial v_j}{\partial x_i} \right)$$

The material constants used in the flow stress model for the 7N01 alloy were taken from reference [24] and are summarized in Table 3.

Table 3. Summary of material constants used in the constitutive model for the 7N01 aluminum alloy base metal.

Property	Value
$A \text{ (s}^{-1}\text{)}$	4.46×10^{13}
$\eta \text{ (Pa}^{-1}\text{)}$	1.18×10^{-8}
n	5.86
Gas constant $R \text{ (J/mol K)}$	8.314
Activation energy $Q \text{ (J/mol)}$	161,000

As heat build-up in the welding tool was not of interest, inter-object heat transfer between the base metal and the pin was not included in the model. However, due to the fact that Fluent partitions the total heat that is generated between the tool and fluid domain, it was necessary to specify the thermal properties of both materials. The material properties of the tool were specified as AISI H13 tool steel and due to the fact that the physical properties do not change significantly over the usual range of aluminum welding temperatures, the

thermal properties were taken to be constant. Thermophysical data for H13 was taken from Ref [27] with a density of 7800 kg/m³, thermal conductivity of 42.0 W/m K, and heat capacity of 440.0 J/kg K.

4.4. Boundary conditions

Based on the consideration that heating results from plastic deformation and friction due to interfacial slipping, the heat flux was calculated according to [18,28,29]:

$$(9) q = \lambda \delta \tau_y \omega r + \lambda (1 - \delta) \mu_f P_0 \omega r$$

Where P_0 is the axial pressure at the tool shoulder, ω is the rotation speed, r is the radius of the integral point, δ is the slip rate, and μ_f is the Coulomb coefficient of friction. Because values of μ_f and δ could not be calculated directly, 0.2 and 0.25 respectively were specified in the simulation model and were found through trial and error. The shear stress, τ_y , was calculated from the yield stress data (shown in Fig. 1) and was updated at the completion of each time step. The percentage of heat transferred into the work-piece λ , is a temperature-based parameter which is a function of the density, thermal conductivity, and heat capacity of the tool and work-piece materials. The value of λ was calculated as:

$$(10) \lambda = \frac{\sqrt{(k\rho C_p)_W}}{\sqrt{(k\rho C_p)_W + (k\rho C_p)_T}}$$

Where the subscripts W and T denote the work-piece and tool, respectively.

A thermal boundary condition was specified on the surfaces of the fluid domain to account for the heat dissipated to the air and the fixture. Convective heat loss was assumed to occur on the top and side surfaces of the plates and the corresponding heat transfer coefficient was specified to be 300 w/(m² K). As contact between the work-piece and fixture mainly occurs at the bottom surfaces of the plates, conductive loss was assumed to occur across the interface and was given by $-h_t \cdot (T - T_{fixture})$, where h_t is the heat transfer coefficient and was prescribed as 500 w/(m² K), T is the temperature on the fluid domain boundary, and $T_{fixture}$ is the fixture temperature. The fixture and air temperature were both assumed to be at ambient and were specified as 300 K.

4.5. Welding parameters and flow characterization

To investigate the relationship between rotation speed, material flow, and defect formation, the experimental weld conditions were simulated along with two intermediate, mid-point values. The latter were used as it was desired to investigate process conditions that corresponded to a transition from a sound weld to those having void defects. A complete summary of the tool rotation speeds that were simulated is given in Table 4.

Table 4. Summary of welding conditions simulated in the Fluent model.

Type	Rotation speed (rpm)	Welding speed (mm/min)	Axial force(N)
Cold welding	200	300	10000
Medium-Low welding	300	300	
Medium welding	350	300	
Medium-High welding	400	300	
Hot welding	500	300	

4.6. Model validation

Prior to simulating each welding condition, the Fluent model was validated using temperatures measurements and marker material images obtained under steady-state conditions for the medium weld condition. The predicted temperatures and thermocouple-measurements for the eight locations shown in Fig. 2 were compared and the results are shown in Fig. 5. Based on Fig. 5, it can be seen that there is good agreement

between the simulated and experimental values. In both cases the temperature distribution was slightly asymmetric and tended to be higher on the advancing side. This is consistent with the fact that more heat is generated on the advancing side of the tool during the welding stage [4]. A slight over-prediction of temperature can be seen at the two locations farthest from the joint centerline and may have resulted from the fact that pre-heating of the material ahead of the tool is not accounted for in the simulation model.

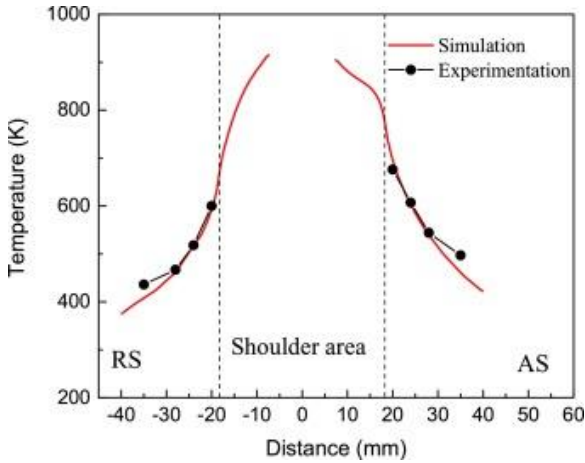


Fig. 5. Comparison of the simulated and experimental temperatures obtained at steady state for the medium weld condition.

In order to validate the simulated material flow, 100 tracer particles were uniformly distributed along a transverse line that was located 5 mm below the top surface of the fluid domain. Because the tracing particles are attached to existing nodes and are assumed to have negligible mass and weight, they will not have any effect on material flow. Results from a CT image of the experimental marker insert and simulated tracer particle distribution at the 5 mm depth were compared for the medium welding condition and are shown in Fig. 6. It can be seen that the material distribution in both cases has the same shape and curvature and demonstrates good agreement. Additional confirmation of the model validity can be obtained by comparing the maximal migration distance which represents the largest distance between the initial and the final positions of a material point. Based on the actual and predicted marker distributions, the maximal migration distances were found to be 11.3 and 14.5 mm, respectively.

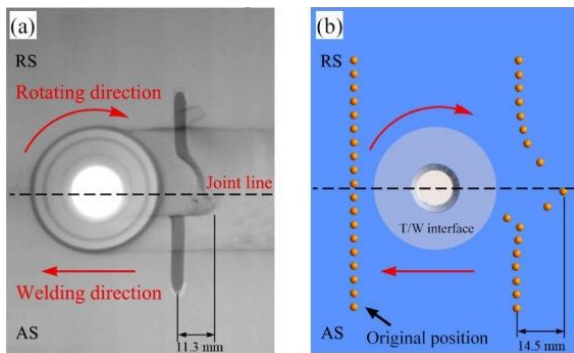


Fig. 6. Comparison of marker material distribution after medium welding obtained by (a) CT imaging and (b) FE simulation.

Due to the intense stirring effect of the pin, the marker insert at the 5 mm depth produced a distorted asymmetric crescent-like shape as shown in Fig. 6. Based on the flow pattern, it can be seen that in the vicinity of the pin that most of the material on both sides of the weld joint had been displaced backwards after the tool had passed. It can be seen that only a small region adjacent to the pin surface on the AS side appears to have experienced a positive or forward displacement. While not evident in the marker material (Fig. 6a), some

evidence of vertical flow can also be seen based on the number of tracer particles shown in Fig. 6b. While 19 tracer particles are shown prior to welding, it can be seen that only 18 particles are present after the tool has passed. The missing particle rotated with the welding tool but translated along the screw in the vertical direction (z-axis). This difference in the number of particles indicates that a longitudinal flow component, as well as a rotational component, operates and drives material flow.

5. Defect analysis

Examining the macrographs of the weld cross-sections shown in Fig. 3, the voids which formed in the CW and HW conditions can be seen to be located in the weld nugget interior. Considering the differences in rotational speed between each of the conditions, it can be inferred that the temperature field had a discernible effect on defect formation. However, considering the differences in type and location, this also implies that the formation mechanism for each void was unique.

5.1. Tunneling voids formation predicted by welding temperature

As the friction between the tool and faying surfaces and intense shear deformation in the adjacent base metal cause the material to undergo adiabatic heating, this band of heated material is often referred to as the plastic zone or plasticized region [12,30]. As illustrated in Fig. 7, the plasticized region consists of heated material and is bounded by cooler base metal material in the radial direction, tool shoulder at the top, and backing plate at the bottom.

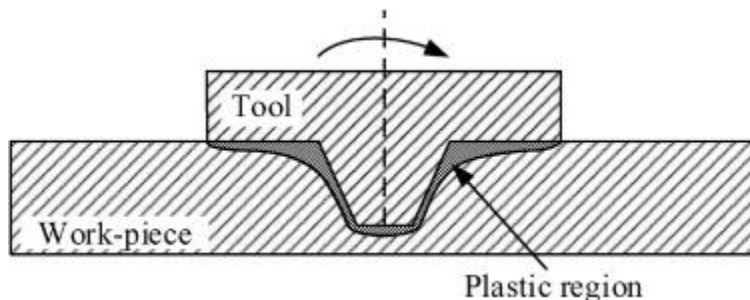


Fig. 7. Schematic illustration of a transverse cross-section showing the plastic region that develops around the welding tool.

Considering that the plasticized material has to achieve a minimum temperature in order to become sufficiently soft and flow around the tool, it is thus useful to demarcate the boundary between the plastic region and surrounding non-plasticized material for analysis purposes. One criterion that can be used to define the plastic zone boundary is based on the characteristic weld microstructure. Within the weld nugget, the material consists of dynamically recrystallized grains in the stir zone while highly distorted but unrecrystallized grains are present in the adjacent thermo-mechanically affected zone. Considering that most engineering metals recrystallize at temperatures above 0.5~0.6 homologous temperature, this provides a convenient means to define the plastic region. As the weld nugget consists of a highly recrystallized grain structure, this suggests that the plasticized region should correlate with the volume of material that is above 0.6 homologous temperature [31].

Although the material in the thermo-mechanically affected zone (TMAZ) will also experience some deformation, due to the lower temperatures and resultant higher flow stress, recrystallization is less likely and substantially less material movement will occur. Examination of Fig. 1(a) provides some support for this as it can be seen that over the hot working region (defined as 0.6 homologous temperature and above), the yield stress begin to flatten out at temperatures greater than 540 K and represents the minimum range of values. Below this temperature range, the yield stress is much higher and the material will be more resistant to deformation. Consequently, the plasticized zone can be defined as a high temperature region (HTR) where the material equals

or exceeds the minimum recrystallization temperature. To be conservative, the HTR was defined in the present study to consist of any material where the temperature was equal to or greater than 570 K (0.65 homologous temperature) during FSW. A representative depiction of a HTR at the top surface of the base metal is shown by the dotted line in Fig. 8.

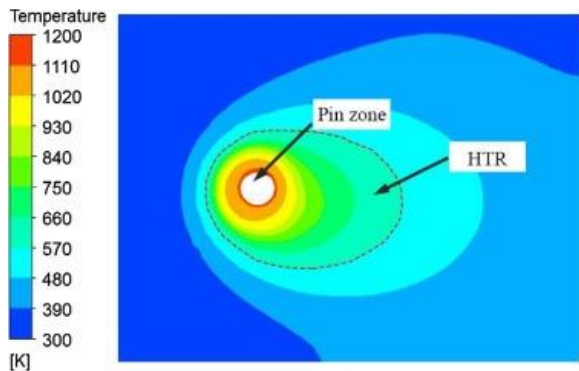


Fig. 8. Schematic illustration showing the simulated high temperature region (HTR boundary is denoted by the dashed line) at the top surface for the HW condition.

As rotation speed is known to have a significant effect on heat generation in FSW, it should also have a strong correlation with HTR size and peak welding temperature. Based on the variation in the nugget over the plate thickness, it is also likely that the HTR cross-section will reflect the same geometry. Fig. 9 shows the HTR cross-sections obtained at depths of 1, 5, and 10 mm for each of the tool rotation speeds that were simulated. These depths were chosen as they correspond to the top, middle, and bottom of the weld joint. It can be seen from Fig. 9 that the HTR shape is circular at all three depths at the lowest rotation speed ($\omega = 200$ rpm). It is also evident that the cross-section and maximum temperature of the HTR shows a noticeable decline with increasing depth and this can be explained as follows. Khandkar, M. et al. [32] showed that maximum heat generation (about 87%) occurs at the shoulder with the remaining amount distributed along the length of the pin. Based on the taper design of the pin, heat generation should decrease in proportion to the pin diameter and the temperature difference is to be expected. This is supported by the results shown in Fig. 10 where the maximum and minimum HTR temperatures and cross-sections are at the shoulder and tip respectively. As rotation speed was changed to 300 rpm, the HTR cross-section and maximum temperature both increased which is consistent with a higher level of heat input. It can also be seen that the difference in HTR cross-sectional area at each depth tended to decrease. The same trend was also observed with further increase in rotational speed though the maximum temperature difference over the plate thickness also increased as seen in Fig. 10. At the highest rotation speed ($\omega = 500$ rpm), the HTR had the maximum cross-section area and the size difference between top and bottom of the joint was relatively small.

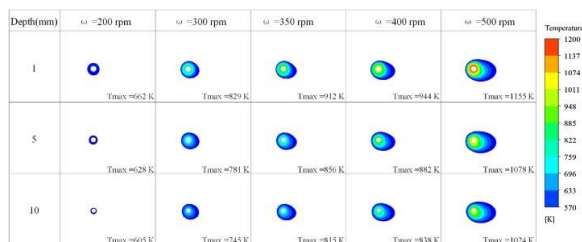


Fig. 9. Variation of HTR cross-section and maximum temperature as a function of tool rotation speed at different depths.

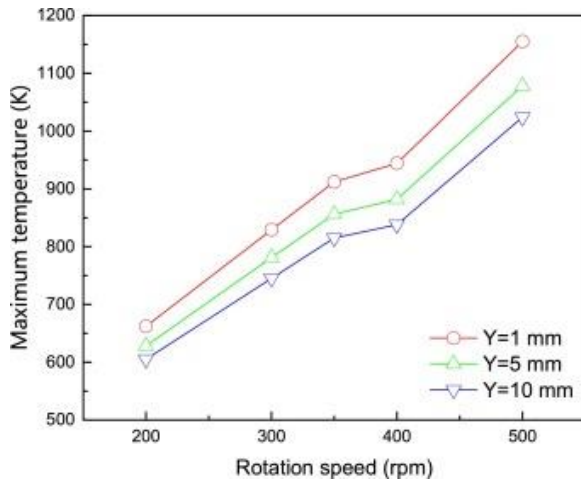


Fig. 10. Maximum HTR temperature obtained at various depths as a function of tool rotation speed.

To better visualize how heat energy was distributed over the plate thickness, HTR cross-sectional area was calculated at 0.2 mm increments from the top surface for each welding condition. Because of the 10° pin taper, the cross-sectional area of the pin will vary with thickness such that the actual or effective HTR area, A_{Eff} , at a given depth will be:

$$(11) A_{Eff} = A_{HTR} - A_{Pin}$$

Where A_{HTR} is the total area contained inside the HTR boundary and A_{Pin} is the cross-sectional area of the pin.

According to the previous discussion, the tunneling void would form since not enough plasticized material to flow and fill space created by pin, and the A_{Eff} represented that how much material in plastic state. To assess the variation of heat for each welding condition, frequency plots were constructed using values of A_{Eff} . The results are shown in Fig. 10 where it can be seen that at the lowest rotation speed (i.e. $\omega = 200$ rpm), all HTR areas were below 750 mm^2 and spread over a wide range. As expected, the smallest HTR areas were concentrated near the tip of the pin. The small size of the HTR zones near the tip of the tool indicates that only a minimal amount of material is plasticized and the faying surfaces are more likely to be extruded rather than stirred by the tool and coalesce together under pressure. As rotation speed was increased to 300 rpm, all of the HTRs increased in area but showed a noticeable decrease in the amount of variation over the plate-thickness. This is consistent with the fact that greater amounts of heat are generated at higher rotational speeds and enables an increase in conductive heat transfer. Further increases in rotational speed also showed a similar trend of larger HTR cross-sectional areas but the spread in HTR area exhibited a minima at $\omega = 350$ rpm. This result is note-worthy as it also coincided with the defect-free medium welding condition. Continued increases in rotation speed then showed an increase in the range of HTR area. However, the frequency plots showed that while most of HTR areas were uniformly distributed for $\omega \leq 350$ rpm, large peaks are evident at rotation speeds of 400 and 500 rpm. Further examination of Fig. 11 shows that the peaks in A_{Eff} occurred near the surface and can be attributed to increased heat generation near the tool shoulder. A second indicator of the tunnel defect can be seen by examining the distribution of A_{Eff} over the plate thickness. Examining Fig. 11 the shape of the curves can be seen to transform from sigmoidal to concave at $\omega=350$ rpm.

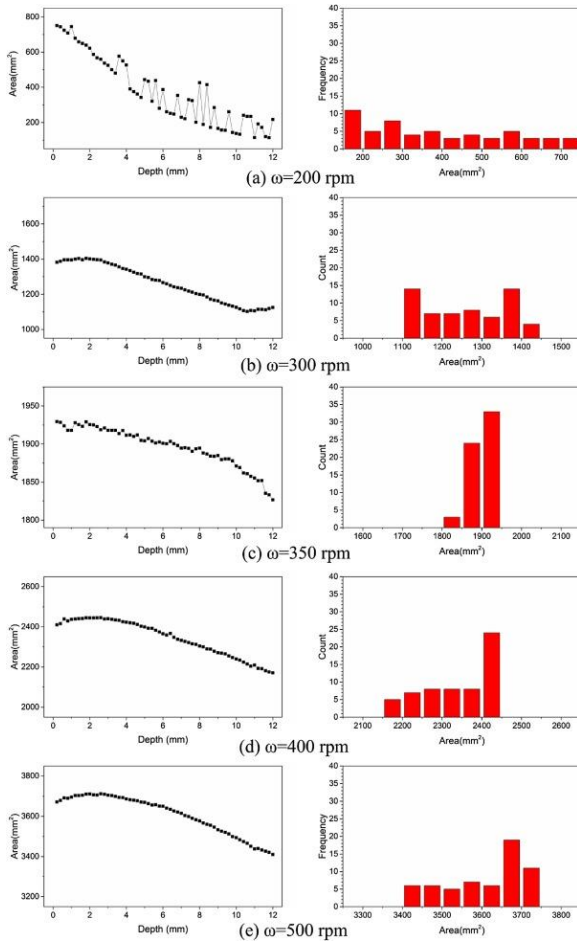


Fig. 11. Distribution and frequency of A_{Eff} at rotation speeds of (a) $\omega = 200$ rpm, (b) $\omega = 300$ rpm, (c) $\omega = 350$ rpm, (d) $\omega = 400$ rpm, and (e) $\omega = 500$ rpm.

To further analyze how the variation in A_{Eff} was related to void formation, the statistical variance was calculated for each weld condition according to Eq 12:

$$(12) \text{Variance} = \sum_{i=1}^n \frac{(A_{i\text{Eff}} - \bar{A}_{Eff})^2}{n}$$

Where $A_{i\text{Eff}}$ is the effective HTR cross-sectional area at a given depth and \bar{A}_{Eff} represents the average of all values obtained from the weld at 0.2 mm increments.

The calculated variance of A_{Eff} for each of the rotation speeds simulated was shown in Fig. 12. Based on the results in Fig. 12, it can be seen that the maximum variance was 40,000 and corresponded to the CW condition. As the rotation speed was increased, the variance dropped to less than 20,000. As expected the minimum variance corresponds to the sound (MW) weld condition. Both of the intermediate conditions show a marked rise in the variance compared to the sound weld. The results indicate that minimal HTR variation is present for a sound weld and that a tunneling defect is more likely to form in a butt weld when significant variability in HTR size exists over the base metal thickness.

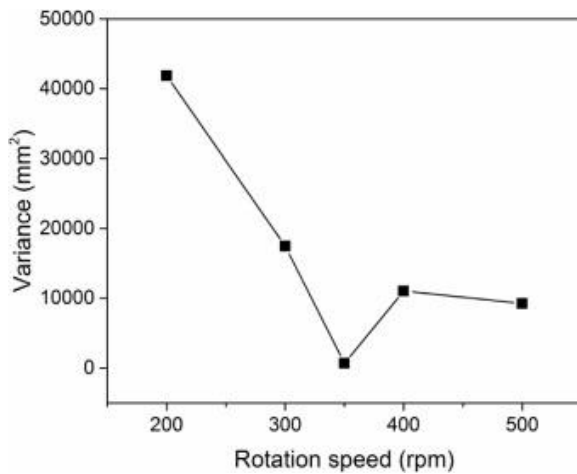


Fig. 12. Variance of A_{Eff} as a function of rotation speed.

However, at the highest rotation speed considered (i.e. $\omega = 500$ rpm), the material temperature is at a maximum and there is a significant volume of plasticized region available. However, the variance is not excessive and a different type of void defect occurred. This suggests that a flow rather than a temperature based formation mechanism is likely responsible for cavity voids and necessitates further analysis.

5.2. Cavity void formation predicted by material flow

As variation in A_{Eff} is an unlikely cause of cavity void formation, additional analysis of material flow was performed by examining tracing particles flowlines obtained from the model and these are shown in Fig. 13. A total of 100 tracing particles were uniformly distributed along a 50 mm long line that was parallel to the Z-axis direction in the Fluent model. The particles were positioned at a distance of 15 mm from the leading edge of the fluid domain and centered about the joint line. For each rotation speed, parallel lines of tracing particles were placed at depths of 1, 2.5, 5, 7.5, and 10 mm from the base metal surface.

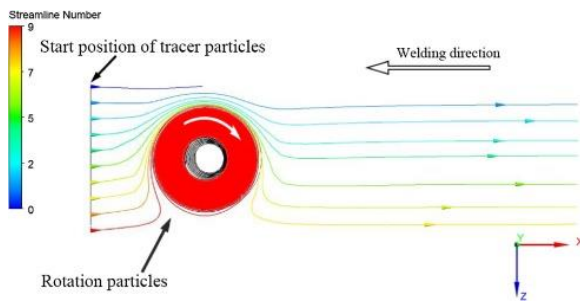


Fig. 13. Tracing particles flow-lines at a 5 mm depth for the MW condition ($\omega = 350$ rpm).

Fig. 14 shows the percentage of rotation particles remaining at each depth after the tool had passed. As rotation speed was increased, the percentage of rotation particles remaining decreased slightly at each depth but the relative distribution over the thick remained almost “constant”. It can be seen that for a given rotation speed that, in general, the percentage of rotation particles showed a marked decrease as the depth increased from 1 to 5 mm. However, at depths from 5 to 10 mm, the difference in percentage of rotation particles was relatively small. However, the one exception to this can be seen for the hot welding condition which showed a significant deviation in the percentage of rotation particles between 5, 7.5, and 10 mm depths, corresponding to the bottom half of the welding tool. This is also noteworthy in that the cavity defect was located 7.8 mm below the surface in the bottom half of the nugget. It can be seen from Fig. 14 that the percentage of rotation particles decreased from about 58% to almost 4% as the depth increased from 5 to 10 mm. As the numbers of particles are conserved in the model, the percent of longitudinal flow at each depth can be estimated by subtracting the

remaining percentage of particles from 100%. This infers that the volume of material rotating with the tool in the bottom half of the plate is sharply reduced and longitudinal flow is predominant.

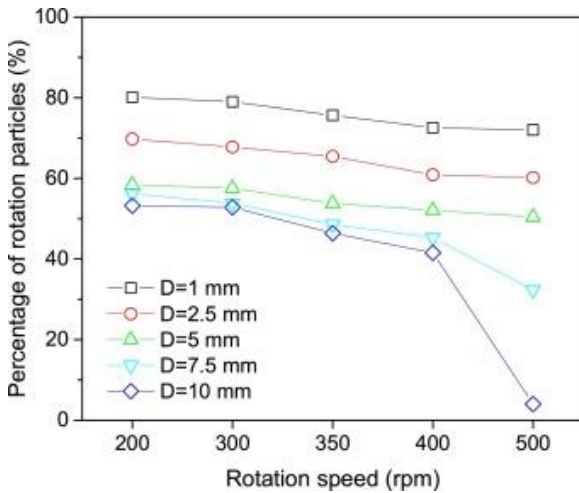


Fig. 14. The percentage of rotation particles observed at various depths shown as a function of tool rotation speeds.

Cavity formation can then be understood by considering the following. It is well established that longitudinal and rotational flow continuity must be maintained to avoid defect formation in FSW. Based on the location of the cavity defect, the results in Fig. 14 indicate that sufficient flow continuity was maintained overall for most of the welding conditions. While there will be some variation in rotational flow near the surface (1–5 mm depth) due to velocity differences on the AS and RS sides, the difference in flow is likely compensated for by compaction from the pin shoulder. While the exception of the HW condition, the rotational and longitudinal flow at the bottom half of the pin (5–10 mm depth) is clustered closely together and is essentially balanced. In comparison, at the HW condition where the cavity defect was observed, it can be considered that velocity differences between the AS and RS will be compensated for as similar compaction will occur at the top half of the nugget (i.e. 1–5 mm depth) due to the shoulder. However, it is evident from Fig. 14 that there is a significant disparity in rotational and longitudinal flow in the bottom half of the pin. It can be surmised that lack of rotational continuity is the probable cause. Some support for this comes from Ke [33] and Qian [34].

6. Conclusion

In the current work, an investigation was conducted to analyze the formation of tunneling and cavity type void defects that developed during FSW of 7N01 aluminum alloy plate. Experimental welds showed that tunneling defects formed at the low rotation speed (cold welding condition) while small cavity voids were present at the highest rotation speed (hot welding condition). A CFD-based process model was developed using the Fluent software and used to simulate butt welding of 12 mm thick plates. The resulting marker material distribution and thermocouple measurements taken from experimental FSW welds showed good agreement with the simulation model and confirmed its validity. Based on the study results, the following conclusions can be drawn:

- (1) Defect free butt welds were obtained in 12 mm thick 7N01 aluminum plate with a conical tool using a constant travel speed of 300 mm/min and rotation speed of 350 rpm.
- (2) The plasticized region was analyzed by defining high temperature regions (HTRs) on the basis of homologous temperature. The variation in HTR cross-sectional obtained from the Fluent CFD model was analyzed and showed that for cold welding the HTR areas have smaller dimension and wider distribution over the plate thickness at lower rotation speeds. This correlated lead to an insufficient amount of plasticized material being generated at the bottom half of the pin and tunnel type void defect formed.

(3) In plane material flow at the hot welding condition was analyzed at various depths using percentage of rotation particles. The percentage of rotation particles around the tool showed a marked decline at 5 mm depth at the highest rotation speed. This indicates a flow disparity which formed a cavity defect.

Acknowledgements

This work was supported by the Fundamental Research Funds for the Central Universities (No. 2018RC004), the National Natural Science Foundation of China (No. 11802011), the National Key R&D Program of China (No. 2017YFB1201302), and National Key Technology R&D Program (No. 2015CB654805) are gratefully acknowledged.

References

- [1] D.C. Hofmann, K.S. Vecchio. **Thermal history analysis of friction stir processed and submerged friction stir processed aluminum.** Mater Sci Eng: A, 465 (1) (2007), pp. 165-175, 10.1016/j.msea.2007.02.056
- [2] F. Al-Badour, N. Merah, A. Shuaib, A. Bazoune. **Coupled Eulerian Lagrangian finite element modeling of friction stir welding processes.** J Mater Process Technol, 213 (8) (2013), pp. 1433-1439, 10.1016/j.jmatprotec.2013.02.014
- [3] M. Dehghani, A. Amadeh, S.A.A. Akbari Mousavi. **Investigations on the effects of friction stir welding parameters on intermetallic and defect formation in joining aluminum alloy to mild steel.** Mater Des, 49 (2013), pp. 433-441, 10.1016/j.matdes.2013.01.013
- [4] R. Igor, Ž Aleksandar, R. Nenad. **Avoidance of tunnel type defect in FSW welded Al 5052-H32 plates.** Zavarivanje i zavarene konstrukcije, 57 (1) (2012), pp. 5-12
- [5] H.S. Park, T. Kimura, T. Murakami, Y. Nagano, K. Nakata, M. Ushio. **Microstructures and mechanical properties of friction stir welds of 60% Cu-40% Zn copper alloy.** Mater Sci Eng a-Struct Mater Properties Microstruct Process, 371 (1-2)(2004), pp. 160-169, 10.1016/j.msea.2003.11.030
- [6] L. Cui, X. Yang, G. Zhou, X. Xu, Z. Shen. **Characteristics of defects and tensile behaviors on friction stir welded AA6061-T4 T-joints.** Mater Sci Eng: A, 543 (2012), pp. 58-68, 10.1016/j.msea.2012.02.045
- [7] L. Fratini, G. Buffa, R. Shivpuri. **Influence of material characteristics on plastomechanics of the FSW process for T-joints.** Mater Des, 30 (7) (2009), pp. 2435-2445, 10.1016/j.matdes.2008.10.014
- [8] Y.G. Kim, H. Fujii, T. Tsumura, T. Komazaki, K. Nakata. **Three defect types in friction stir welding of aluminum die casting alloy.** Mater Sci Eng: A, 415 (1-2) (2006), pp. 250-254, 10.1016/j.msea.2005.09.072
- [9] H.I. Dawood, K.S. Mohammed, A. Rahmat, M.B. Uday. **Effect of small tool pin profiles on microstructures and mechanical properties of 6061 aluminum alloy by friction stir welding.** Trans Nonferrous Metals Soc China, 25 (9) (2015), pp. 2856-2865, 10.1016/S1003-6326(15)63911-5
- [10] P.A. Colegrove, H.R. Shercliff. **3-Dimensional CFD modelling of flow round a threaded friction stir welding tool profile.** J Mater Process Technol, 169 (2) (2005), pp. 320-327, 10.1016/j.jmatprotec.2005.03.015
- [11] P.A. Colegrove, H.R. Shercliff, R. Zettler. **Model for predicting heat generation and temperature in friction stir welding from the material properties.** Sci Technol Weld Join, 12 (4) (2007), pp. 284-297, 10.1179/174329307x197539
- [12] H. Wang, P.A. Colegrove, J.F. dos Santos. **Numerical investigation of the tool contact condition during friction stir welding of aerospace aluminium alloy.** Comput Mater Sci, 71 (Suppl. C) (2013), pp. 101-108, 10.1016/j.commatsci.2013.01.021
- [13] T. Long, A.P. Reynolds. **Parametric studies of friction stir welding by commercial fluid dynamics simulation.** Sci Technol Weld Join, 11 (2) (2006), pp. 200-208, 10.1179/174329306X85985
- [14] X. Pei, P. Dong. **A selectively-coupled shear localization model for friction stir welding process window estimation.** Int J Mach Tools Manuf, 123 (Suppl. C) (2017), pp. 89-104, 10.1016/j.ijmachtools.2017.08.003

- [15] B.C. Liechty, B.W. Webb. **Modeling the frictional boundary condition in friction stir welding.** *Int J Mach Tools Manuf*, 48 (12) (2008), pp. 1474-1485, 10.1016/j.ijmachtools.2008.04.005
- [16] Y. Zhu, G. Chen, Q. Chen, G. Zhang, Q. Shi. **Simulation of material plastic flow driven by non-uniform friction force during friction stir welding and related defect prediction.** *Mater Des*, 108 (2016), pp. 400-410, 10.1016/j.matdes.2016.06.119
- [17] N. Rajamanickam, V. Balusamy, G. Madhusudhanna Reddy, K. Natarajan. **Effect of process parameters on thermal history and mechanical properties of friction stir welds.** *Mater Des*, 30 (7) (2009), pp. 2726-2731, 10.1016/j.matdes.2008.09.035
- [18] H. Schmidt, J. Hattel, J. Wert. **An analytical model for the heat generation in friction stir welding.** *Modell Simul Mater Sci Eng*, 12 (1) (2004), p. 143
- [19] W.J. Arbegast. **A flow-partitioned deformation zone model for defect formation during friction stir welding.** *Scripta Materialia*, 58 (5) (2008), pp. 372-376, 10.1016/j.scriptamat.2007.10.031
- [20] Y.H. Zhao, S.B. Lin, Z.Q. He, L. Wu. **Microhardness prediction in friction stir welding of 2014 aluminium alloy.** *Sci Technol Weld Join*, 11 (2) (2006), pp. 178-182, 10.1179/174329306x84391
- [21] A. Ajri, Y.C. Shin. **Investigation on the effects of process parameters on defect formation in friction stir welded samples via predictive numerical modeling and experiments.** *J Manuf Sci Eng*, 139 (11) (2017), pp. 111009-111010, 10.1115/1.4037240
- [22] S.D. Ji, Q.Y. Shi, L.G. Zhang, A.L. Zou, S.S. Gao, L.V. Zan. **Numerical simulation of material flow behavior of friction stir welding influenced by rotational tool geometry.** *Comput Mater Sci*, 63 (2012), pp. 218-226, 10.1016/j.commatsci.2012.06.001
- [23] Z. Yu, W. Zhang, H. Choo, Z. Feng. **Transient heat and material flow modeling of friction stir processing of magnesium alloy using threaded tool.** *Metallur Mater Trans A*, 43 (2) (2012), pp. 724-737, 10.1007/s11661-011-0862-1
- [24] J. Tang, Y. Shen. **Numerical simulation and experimental investigation of friction stir lap welding between aluminum alloys AA2024 and AA7075.** *J Alloys Compd*, 666 (2016), pp. 493-500, 10.1016/j.jallcom.2016.01.138
- [25] O.C. Zienkiewicz, I.C. Corneau. **Visco-plasticity—plasticity and creep in elastic solids—a unified numerical solution approach.** *Int J Numerical Methods Eng*, 8 (4) (1974), pp. 821-845, 10.1002/nme.1620080411
- [26] T. Sheppard, A. Jackson. **Constitutive equations for use in prediction of flow stress during extrusion of aluminium alloys.** *Mater Sci Technol*, 13 (3) (1997), pp. 203-209, 10.1179/mst.1997.13.3.203
- [27] H. Su, C.S. Wu, M. Bachmann, M. Rethmeier. **Numerical modeling for the effect of pin profiles on thermal and material flow characteristics in friction stir welding.** *Mater Des*, 77 (2015), pp. 114-125, 10.1016/j.matdes.2015.04.012
- [28] R. Nandan, G.G. Roy, T. Debroy. **Numerical simulation of three-dimensional heat transfer and plastic flow during friction stir welding.** *Metall Mater Trans A-Phys Metall Mater Sci*, 37A (4) (2006), pp. 1247-1259, 10.1007/s11661-006-1076-9
- [29] R. Nandan, G. Roy, T. Lienert, T. Debroy. **Three-dimensional heat and material flow during friction stir welding of mild steel.** *Acta Materialia*, 55 (3) (2007), pp. 883-895
- [30] G. Buffa, G. Campanile, L. Fratini, A. Prisco. **Friction stir welding of lap joints: influence of process parameters on the metallurgical and mechanical properties.** *Mater Sci Eng: A*, 519 (1) (2009), pp. 19-26, 10.1016/j.msea.2009.04.046
- [31] W.F. Xu, J.H. Liu, D.L. Chen, G.H. Luan, J.S. Yao. **Improvements of strength and ductility in aluminum alloy joints via rapid cooling during friction stir welding.** *Mater Sci Eng: A*, 548 (2012), pp. 89-98, 10.1016/j.msea.2012.03.094
- [32] M. Khandkar, J. Khan, A. Reynolds. **Prediction of temperature distribution and thermal history during friction stir welding: input torque based model.** *Sci Technol Weld Join*, 8 (3) (2003), pp. 165-174, 10.1179/136217103225010943

- [33] L. Ke, L. Xing, J.E. Indacochea. **Material flow patterns and cavity model in friction-stir welding of aluminum alloys.** Metallur Mater Trans B, 35 (1) (2004), pp. 153-160, 10.1007/s11663-004-0105-6
- [34] J. Qian, J. Li, F. Sun, J. Xiong, F. Zhang, X. Lin. **An analytical model to optimize rotation speed and travel speed of friction stir welding for defect-free joints.** Scripta Materialia, 68 (3–4) (2013), pp. 175-178, 10.1016/j.scriptamat.2012.10.008